ORIGINAL ARTICLE

High temperature effects on the properties of limestones: post-fire diagnostics and material's durability

Martin Vigroux · Francesca Sciarretta ⬤ · Javad Eslami · Anne-Lise Beaucour ·
Ann Bourgès · Albert Noumowé

Abstract The research aims at investigating the temperature dependency of important properties of construction limestones, in the temperature range that could be reached during fires (200–800 °C). Limestones, through their different species and geographical origins, show a great variability in basic properties. The presented data will be useful to the post-fire recovery design of stonework buildings, by supporting the judgement on the perspects of durability based on the post-fire state of stones. The research features six varieties of construction limestones from different zones of France. The tests—colorimetry, ultrasonic P-wave velocity, total porosity, mercury intrusion porosimetry (MIP), scanning electron microscope (SEM) observations, capillary water absorption—are performed after high temperature exposure in a controlled furnace oven. The samples and heating conditions are designed to attain a uniform maximum temperature inside the samples. Nondestructive investigation techniques have a great potential usefulness in the perspect of post-fire investigations; on the other hand, the changes in the porous network, porosity and capillarity—investigated in laboratory—are direct indicators of post-fire materials' decay. The individuated temperature-property relationships of the single stone species, as well as correlations between P-wave velocity to porosity and compressive strength, are generally reliable. Finally, the detrimental effect of post-cooling rehydration has been observed through the kinetics of deterioration for all the investigated varieties of limestone. The results demonstrate the need of integrating non-destructive techniques to laboratory tests for cost-effective diagnostics on fire-damaged stonework buildings.

Keywords Limestone · High temperature · Colorimetry · Microstructure · Mechanical properties · Thermal alteration

M. Vigroux · F. Sciarretta (✉) · J. Eslami ·
A.-L. Beaucour · A. Noumowé
Laboratoire de Mécanique et Matériaux du Génie Civil,
CY Cergy Paris Université, 95000 Cergy, France
e-mail: scifra@iuav.it

A. Bourgès
Laboratoire de Recherche des Monuments Historiques,
Ministère de la Culture et de la Communication, 29 Rue
de Paris, 77420 Champs-Sur-Marne, France

A. Bourgès
Centre de Recherche Sur la Conservation (CRC, USR
3224), Sorbonne Universités, Muséum National d'Histoire
Naturelle, Ministère de la Culture et de la
Communication, CNRS, CP21, 36 Rue Geoffroy-Saint-
Hilaire, 75005 Paris, France

1 Introduction

Monuments, as well as traditional buildings, are an essential part of communities' tangible cultural heritage. Against time-dependent decay, natural

calamities and man-made hazards, strategies for the preservation of monuments are discussed, elaborated and made effective all over the world, in the interest of citizens [1]. Throughout the richest Countries in pre-1900s cultural heritage buildings, stonework is the most common material that monuments are made of [2, 3].

The aftermath of a severe fire in a stonework building often means a very slow recovery, or a long period of disruption [4, 5]. For monuments, considerable effort is required by the post-fire assessment of complex structural systems. In particular, the considerable variety of construction stones in historic buildings demands a thorough identification of the material. In France, and in most of Central Europe as well, limestones are very common as materials for stonework, both historic and contemporary [6, 7]; moreover, historic mortars are lime-based.

Typical thermal ranges experienced by stone masonry members in cellulosic fuel fires—the most likely in historic buildings—are 200–1000 °C. Up to 600 °C, the thermal damage of limestones is largely due to the strongly anisotropic thermal expansion of calcite—positive along the crystallographic c-axis and negative in the perpendicular directions—that causes intergranular microcracking [8, 9].

Stones undergo temperature-dependent chemical-physical changes, whose macroscopic consequences—cracking, mechanical decay and increase in porosity—affect the residual structural capacity and durability of the building after the fire. According to the relevant state-of-the-art, such phenomena are quite well known [10]. The behaviour of lime-based rocks is mainly affected by two processes. In the heating phase (650–950 °C), calcite ($CaCO_3$) transforms into quicklime and carbon dioxide (decarbonisation, Eq. 1); this transformation is also affected by the partial pressure of CO_2, which is likely to be high during fires. The related endothermal reaction leads to significant mass loss. After the decarbonisation in the heating phase (with temperatures exceeding 650 °C), the presence of water—e.g. hose stream for fire extinguishment—or air humidity triggers the rehydration of quicklime (Eq. 2). The formation of portlandite ($Ca(OH)_2$) as the product of rehydration entails considerable volumetric expansion of the material.

$$CaCO_3 \rightarrow CaO + CO_2 \qquad (1)$$

$$CaO + H_2O \rightarrow Ca(OH)_2 \qquad (2)$$
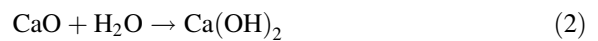
In addition to calcite—that is present for more than the 50% in volume—other minerals could affect the behaviour of limestones under high temperatures. Dolomite decarbonises approximately along the same temperature range as calcite. Clay minerals undergo dehydroxilation (eventually forming hematite, which gives a typical reddish colour) from 200 to 800 °C; quartz-α turns to quartz-β at 573 °C, and it reverts at cooling; finally, gypsum dehydrates with exothermal reactions (100–300 °C).

The investigation of the post-cooling state of stones subjected to high temperatures is essential to assess the residual capacity of buildings/monuments to be restored. In the perspective of the service life after a fire event, several material properties need to be investigated. A thorough diagnostic should compare the initial state and the post-cooling state, as a function of the experienced temperature in different zones of the building. Ideally, on site non-destructive investigations (providing qualitative information) should go along with destructive tests in laboratory tests on material samples (providing quantitative information) [11].

Non-destructive measurements of ultrasonic P-wave velocity allow detecting the intensity of cracking within a material portion; it can be easily applied also on site, on wide portions of the damaged building, at very low cost [12, 13]. The colour change gives useful indications about the maximum temperature withstood by a stone; non-destructive colorimetric tests measure the changes in colour associated to peculiar minerals' transformations [14].

To obtain a picture of the residual strength of the material in the different parts of the building, such qualitative information should be supported by quantitative figures from mechanical tests. The latter must be limited, due to the need of destroying a significant number of small samples. It is worth noting that specific mechanical testing protocols for masonry materials after high temperature exposure are not available. Testing protocols that use heating to induce an artificial weathering in stones are available [15, 16]; however, such standard heating procedures involve several subsequent heating cycles, which are not comparable to a fire exposure. RILEM [17] provides recommendations for concrete testing at high temperatures, which were adopted in previous studies [18].

According to the state-of-the-art, the visual assessment of macroscopic thermal crack pattern can be supported by Scanning Electron Microscope (SEM) observations on stone fragments, to identify the nature of microcracks [19]. Moreover, the increased porosity of a rock after exposure to high temperatures is related to the maximum experienced temperature [20, 21]; it can be measured as the porosity accessible to water, by standard tests [22]. The absorption and transport of water within a material sample are determined by the material's pore size distribution. Capillary water absorption tests apply to small samples, according to available protocols [23, 24]. Mercury Intrusion Porosimetry (MIP) requires material fragments to assess the pore radius distribution; it can be corroborated by the observation of pores through SEM [25, 26].

The paper presents experimental results that will be useful in construing an integrated diagnostic strategy—based on non-destructive investigations and experimental information, like it was proposed in other cases [27–29]—for limestone masonry buildings after fire events. The results and empirical relationships presented in the following sections will be useful to the judgement of residual stability and prospects of durability based on the post-fire state of the stones. The research focuses on six limestones from France; although the general features of the behaviour of limestone under high temperatures are well-known, this stone type displays a high variability of main properties across its species. For this reason, the choice of materials encompasses a wide range of basic physical, mechanical and microstructural properties and covers a large geographical area.

2 Materials and methods

2.1 French limestones

The six limestones used in this study came from active quarries in different regions of France: Massangis (MA), Lens (LS), Euville (EUV), Migné (MI), Saint Maximin (MX), and Savonnières (SA). These stones are very common in historical monuments and are still used for restoration [30, 31]. They encompass a variety of physical, mechanical and petrographic properties. Table 1 lists the open porosity N_T, compressive strength R_C, capillary absorption coefficient

A and P-wave velocity V_p, the macroscopic description and the mineralogical composition, as enlightened by XRD analyses (Sect. 3.1). A preliminary study with polarized light microscope allowed to establish the rocks' classification according to Dunham [32].
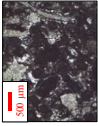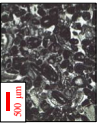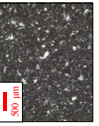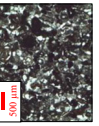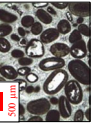
As for the size of the basic samples, indications about the Representative Elementary Volume (REV) of similar materials were considered [33], choosing a cylindric shape of 4 cm diameter and 8 cm height. The samples were cored out of blocks, sawn, washed, dried at 80 °C for 72 h and stored in a controlled room at 20 °C and 50% relative humidity.

The whole batch of materials served a wide experimental programme, the first results of which have already been published [18]. In particular, the values of uniaxial compressive strength of the investigated stones, as a function of maximum temperature, are summarised in Table 7 (Appendix).

2.2 Heating and testing procedures

Since the main objective of the study is to establish the evolution of the material decay and properties as a function of temperature, it is essential to ensure the temperature homogeneity through the sample, and to limit the cracks development due to thermal gradients. A 4 °C/min heating rate was established according to RILEM recommendations for concrete samples [17], which suggest rate values relating to the diameter of the sample, to avoid radial temperature differences of more than 20 °C. The chosen heating rate is much lower than the one of the standard curve ISO 834 for simulation of fires from cellulosic fuel (around 20 °C/min in the first 30 min), as well as than the rates usually applied in other types of fire-related investigation, for instance spalling [34]. In fact, to the aim of investigating the temperature-dependent properties of the considered materials, it is essential to choose a low heating rate, to allow for uniform temperature distribution within the sample and to avoid possible cracking due to high thermal gradients. Then, the duration at constant maximum temperature was set to 1 h, to ensure that the samples uniformly reached the maximum temperature. In fact, the preliminary tests that had indicated only small temperature differences between surface and core, which can be considered null after a 1 h duration. The selected temperature targets are likely to be reached through the phases of a real fire; they were also chosen with reference to

Table 1 Characteristics of the investigated materials

ID	NT (%)	RC (N/mm²)	Vp (m/s)	A (g/(m²√s))	Structure	Cohesion	Fracture	Texture	Colour	Mean grain size (μm)	Composition* C	D	Q	H	Microphotograph	Dunham's Classification
MA	11.2 ± 0.5	74.5 ± 1.5	4941 ± 192	23 ± 6	Anisotropic	Consolidated	Granular	Feebly porous, heterogranular	Beige	625 ± 392	+++	++	+	+		Oolitic/peloidal grainstone
LS	15.4 ± 0.8	27.5 ± 1.5	4380 ± 172	48 ± 3	Anisotropic, nodular	Friable	Granular	Porous, isogranular	White	300 ± 89	+++	–	–	–		Bioclastic grainstone
EUV	17.2 ± 0.4	20.0 ± 1.0	3665 ± 359	73 ± 5	Anisotropic, granular	Friable	Granular	Porous, heterogranular	Beige, orange	1337 ± 610	+++	–	–	+		Bioclastic (crinoidal) grainstone
MI	26.8 ± 0.8	20.1 ± 3.1	3138 ± 95	224 ± 15	Isotropic	Friable	Undefined	Feebly porous, isogranular	White	68 ± 17	+++	–	–	+		Peloidal packstone
MX	29.7 ± 1.2	15.5 ± 1.2	2971 ± 124	209 ± 11	Anisotropic	Friable	Granular	Porous, heterogranular	Grey, beige	309 ± 131	+++	–	+	–		Bioclastic packstone
SA	30.7 ± 1.3	9.4 ± 0.6	2984 ± 119	73 ± 15	Anisotropic, nodular	Friable	Granular	Very porous, heterogranular	Grey, beige	526 ± 180	+++	–	–	–		Oolitic grainstone

*C: calcite; D: dolomite; Q: quartz; H: hematite; +++: dominantly present; ++: present; +: traces; –: not present

specific temperatures of chemical-physical transformation of limestones under high temperature exposure. Finally, the samples were left cooling slowly, inside the closed oven; in this way, the effect of thermal shock is excluded from the simulation.

An electric furnace with a 1.35 m³ capacity (1.12 m long, 1.20 m in depth and 1.00 m high), available at the Laboratory of Mechanics of Materials in Civil Engineering (L2MGC) at CY Cergy Paris University was used. The two side walls are equipped with heating resistors and a ventilator to maintain a homogeneous temperature distribution. For each thermal cycle, six samples (cylinders of 8 × φ4 cm) were equipped with one K-type thermocouple on the surface and one at the centre of the sample's cross section, at mid-height. The latter was inserted through a 3 mm hole and fixed at the core of the sample with a specific glue; the hole was then filled with powdered stone. The two thermocouples allow measuring the thermal gradient between the surface and the core, and checking that the samples attain each target temperature in an acceptably uniform way. In fact, a preliminary thermal response test on samples exposed to a 600 °C cycle demonstrated that, at the peak temperature, the difference between the surface and core temperature was between + 20 and + 10 °C [18]. Other 10 thermocouples are placed on different zones inside the oven, as well as on the surfaces of different samples, to ensure homogeneous air temperature, and thus uniform exposure of all the samples in the same heating cycle.

Four different high temperature treatments were applied on samples through heating–cooling cycles: from room temperature up to 200, 400, 600 and 800 °C. Each thermal treatment includes a 4 °C/min heating phase up to target temperature, then a one-hour isotherm stage and finally a semi-forced cooling phase. The choice is again based on the RILEM recommendations for concrete [17].

2.2.1 X-ray diffraction (XRD)

X-ray diffraction (XRD) is a non-destructive technique to identify and evaluate the minerals present in very small samples of the investigated materials. The analyses were carried out on a Brucker diffractometer, to establish the mineralogical composition of the investigated stones. The analyses were conducted on fragments, previously dried in an oven (80 °C for 72 h), and then reduced to powder by using a grinder. Three tests were performed for each type of stone in order to ensure the homogeneity of the batch. The obtained diffraction diagrams were applied a quantitative analysis of the relative proportion of phases, following Rietveld's method [35]. The XRD analyses were performed on samples before exposure and after exposure to 600 and 800 °C.

2.2.2 Open porosity accessible to water: test under vacuum

The total porosity (N_T), i.e. the total volume fraction of pores that can be filled with water under vacuum, was determined according to standard NF EN 1936 [22]. At different stages of the procedure, it is possible to measure the dry mass of the samples (m_{dry}, just after drying in the oven), the hydrostatic mass (m_{hyd}, measured in water after the 24 h immersion), and the saturated mass (m_{sat}, just out of the water, after drying the surfaces). These parameters determine the total porosity N_T, according to Eq. 3, where V_v is the volume of voids and V_{tot} is the total volume. The tests were performed on non-exposed samples, as well as after exposure to 200, 400 and 600 °C.

$$N_T = \frac{m_{sat} - m_{dry}}{m_{sat} - m_{hyd}} \times 100 = \frac{V_v}{V_{tot}} \times 100 \qquad (3)$$

2.2.3 Mercury intrusion porosimetry (MIP)

MIP tests were performed to investigate the pore size distribution of the stones. This method is based on capillary equilibria between mercury and its vapor phase in the pore network. The test consists of an injection of mercury under controlled pressure to allow it to penetrate the medium. The incremental increase in pressure allows access to very fine pore sizes. Assuming the pores are cylindric, Eq. 4 relates the access radius of the pores filled with mercury to the applied pressure.

$$r = \frac{2\sigma_{Hg}\cos\theta}{P} \qquad (4)$$

In Eq. 4, r is the pore radius in m, σ_{Hg} the surface tension of mercury (= 0,485 N/m), θ the contact angle between the solid surface and the mercury (= 130°), and P the applied pressure in Pa. Thus, a maximum pressure of 206 MPa obtained during the test gives

access to pores with a radius between 0.003 and 200 μm.

The freeze-drying (lyophilisation) of samples drying is a common preparation procedure prior to the SEM observation [36]. It allows to completely remove the sample's water content at the solid state, with a vacuum pump. It prevents any particles movement, mainly due to shrinkage, contrarily to air and oven drying techniques [37]. The tests were carried out with a Micrometrics Autopore IV series 9500 device on stone fragments (about 1 cm³). The MIP measurements were performed on small fragments (about 1 cm³) taken from the cores of the samples, previously dried in an oven at 80 °C for 72 h. Three samples were tested for each type of stone to ensure the representativeness of the results. The tests were performed on non-exposed samples, as well as after exposure to 400 and 600 °C.

2.2.4 Scanning electron microscope (SEM) observations

The SEM observations were performed on a ZEISS GeminiSEM 300 device, at a variable electron beam intensity depending on the type of observation and an acceleration voltage ranging between 2 and 1 kV. The observations were carried out on fragments of stone, previously freezed down to − 50 °C for 48 h; the frozen water contained in the fragments was cleared off by means of a vacuum pump. The tests were performed on non-exposed samples, and after exposure to 600 °C.

2.2.5 Measurement of ultrasonic wave velocity

The measurement of velocity of primary ultrasonic waves (P-wave velocity V_P) corresponding to compression waves, is a non-destructive technique. The characterisation it gives relies on the effect of porosity and cracking on the wave propagation inside the investigated sample. Measurements were performed using a Pundit7 test device from Pundit Lab, according to standards NF EN 14579, paying attention to attain a dry state in the samples [38]. The frequency of the solitary pulse in this experiment was 54 kHz. The average values for each stone are based on 60 samples for initial state and on 10 samples after each high temperature (40 specimens in total per stone).

2.2.6 Capillary water absorption

This test was performed according to standards NF EN 1925 on cylindrical specimens (Φ40 × 80 mm), previously dried in an oven at 80 °C for 72 h. The principle is based on the fact that when a porous material is brought into contact with water, the non-wetting fluid (air) that filled the pores is displaced by the wetting fluid (water) without any external pressure being applied. The capillary imbibition depends on the size and connectivity of the pores in the stone, but also on the properties of the fluid. Under the hypothesis of a steady state flow of a Newtonian fluid through a cylindrical tube of radius R, the Washburn equation applies (Eq. 5)

$$dW/S = A \cdot t^{1/2} = \pi r^{5/2} \sqrt{\frac{\sigma_{lv} \cos \theta}{2\eta}} \cdot t^{1/2} \qquad (5)$$

with dW/S mass of water increase per unit surface of the immersed base of the specimen in g/m²; A capillarity coefficient in g/(m²√s); t time in s; R pore radius in m; σ_{lv} interfacial tension between liquid and vapour; θ angle contact between solid and liquid in °; η dynamic viscosity of the fluid in Pa·s. The tests were performed on non-exposed samples, as well as after exposure to 400 and 600 °C. The mean values came from six samples per case.

2.2.7 Colorimetry

The three most commonly studied colorimetric parameters, L^*, a^* and b^* are associated with the CIELAB color space. This 3D space is inscribed in a slightly flattened sphere where the vertical axis L^*, corresponds to the lightness, or scale of neutrals, according to a psychiometric scale going from 0 to 100—i.e. from black or total absorption to white or total reflection. In each horizontal plane of the sphere, at any value of lightness L^*, two orthonormal axes are used to position the coordinates of chromaticity: the axis − a^*/ + a^* for green and red, and the axis − b^*/ + b^* for blue and yellow.

The colorimetric characteristics of the selected stones were determined at intial state and after the four different high temperature treatments. The device used was a Konica Minolta colorimeter CM-2300d: it has an integrating sphere of Φ52 mm, and displays a spectral resolution of 10 nm. A white ceramic was

provided and used as reference material for the calibration of the instrument. The results are based on three specimens per stone, with four measurements per specimen.

3 Results and discussion

3.1 Mineralogical characterisation (XRD)

The XRD analyses on dried samples grinded to powder have provided diffractograms describing the overall mineralogical composition. The heating–cooling cycles up to 600 °C have almost no effect on the mineralogical composition of the investigated limestones. In fact, the related diffractograms show no significant difference from those of the unheated specimens. The only exception is the MA stone, which shows a decrease of peaks associated to dolomite after the exposure to 600 °C; the peaks are completely flattened after the 800 °C cycle. For all the other types, the diffractograms after the 800 °C cycle show the same feature, that is the remarkable flattening of the calcite peaks, and the appearance of lime and portlandite. An example is shown in Fig. 1a, where 2 Theta is the angle between the incident and the reflected beam.

Lime is the product of calcite decomposition according to Eq. 1; the presence of small peaks of calcite after 800 °C is due to the fact that the decomposition is generally completed at 930 °C. Finally, the formation of portlandite, visible in Fig. 1b, is the result of the decarbonisation of calcite followed by hydration due to the air humidity while cooling down. Other minerals, notably iron

compounds, have not been detected by XRD, due to extremely low quantity, or to presence in amorphous phases [39].

The exposure procedure was aimed to attain a uniform maximum temperature in the whole sample (Sect. 2.2); this nonetheless resulted in a non-homogeneous consistency of samples after cooling, when the maximum temperature was 800 °C (Fig. 2b), due to the physical–chemical transformations induced by the environment during cooling (formation of portlandite).

3.2 Open porosity accessible to water

As already demonstrated for marbles by Koca et al. [20], a correlation can be found between residual total porosity and experienced temperature (Fig. 2).

The linear trends plotted in Fig. 2 (dotted lines) show satisfying correlations between total porosity and temperature, for all the investigated types of stone. In particular all the linear trends $N_T(T) = mx + q$ have determination coefficient $R^2 \geq 0.92$ (Table 2). Whenever porosity tests—which are moderately destructive, as they require the extraction of samples from the masonry—are planned, such formulations would be useful in corroborating the non-destructive evaluations of the experienced temperature from colorimetry.

Figure 3 shows the evolution of the absolute increase in the open porosity accessible to water (N_T) as a function of temperature. The measurement was not performed on the samples that underwent the heating–cooling cycle at 800 °C because of the excessive deterioration of the material. At the 200 °C level, the absolute increase in total porosity
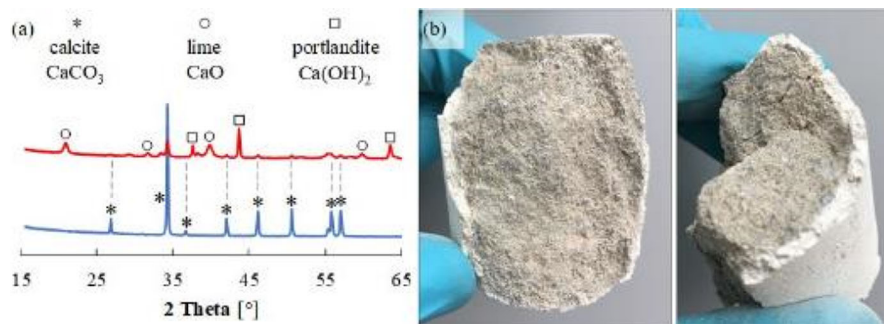

Fig. 1 a XRD analyses: evolution of mineralogical composition for MI limestone at initial state (blue line) and after an 800 °C heating–cooling cycle (red line); **b** LS sample after an 800 °C heating–cooling cycle: formation of portlandite on surface and development towards the core. (Color figure online)

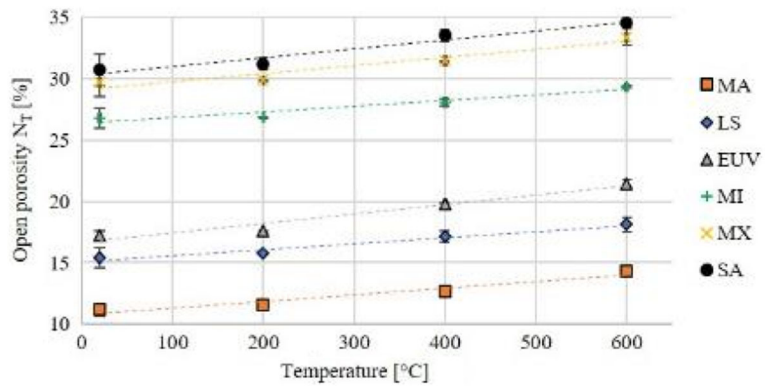**Fig. 2** Graphs of total porosity N_T versus temperature T

Table 2 Coefficients of the parameter trends for the N_T–T relationships (Fig. 2)

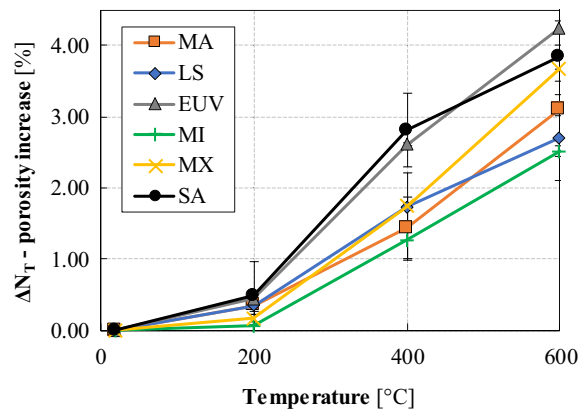| ID	$N_T(T) = mT + q$		
	m	q	R^2
MA	5.4×10^{-3}	10.779	0.938
LS	4.9×10^{-3}	15.099	0.966
EUV	7.7×10^{-3}	16.667	0.958
MI	4.5×10^{-3}	26.377	0.919
MX	6.5×10^{-3}	29.100	0.919
SA	7.2×10^{-3}	30.301	0.952

Fig. 3 Evolution of porosity increase as a function of temperature up to 600 °C

does not exceed 0.50% for all limestones. A clear increase ($\sim$ 2.50–3.00%) is displayed at 400 °C for EUV and SA limestones, while it is smaller for the rest of the stones ($\sim$ 1.35–1.80%). MX as well shows a strong increase, with a total porosity gain value of

around 4.00%. The absolute value of the increase in total porosity for MA is 3.00% at 600 °C, and around 2.50% for LS and MI stones, which show the smallest increase.

3.3 Pore size distribution (MIP)

The pore size distribution at the original state is analysed first of all. Table 3 presents the main parameters resulting from the MIP measurements at the original state.

As noticed by Walbert [40], the values of porosity N_{Hg} are systematically lower than N_T, but nonetheless they retain the same classification and order of magnitude. Equation 6 expresses the coefficient of dispersion C_D

$$C_D = \frac{P_{80} - P_{20}}{P_{50}} = \frac{r_{80} - r_{20}}{r_{50}} \qquad (6)$$

where P_{80}, P_{20} and P_{50} are the mercury pressures corresponding to the filling of the 80, 20 and 50% of the pore volume. The relationship among pressures can be transposed to the corresponding pore radiuses. For $C_D < 1$, the pore distribution is unimodal and the values of r concentrate in a single pore family, while $C_D < 1$ may indicate bimodal or multimodal as well as unimodal but scattered distributions [41]. The characteristic diameter d_{peak} is associated to the highest amount of mercury injected. Finally, the pore network of a stone may be subdivided in three categories. The first, characterized by $r_1 < 0.1$ μm, corresponds to the pores where capillary condensation occurs; then, the capillary imbibition involves pores of radii 0.1 μm $< r_2 <$ 10 μm; finally, pores of radius $r_3 >$ 10 μm are associated to fluids transport according to Darcy's law.

Table 3 Parametres of the pore network of the stones at the original state

ID	NHg (%)		CD (–)	dpeak (μm)	Share of pore familes (%)		
	Mean	CoV (%)			r1 < 0.1 μm	0.1 μm < r2 < 10 μm	10 μm < r3
MA	9.8 ± 0.7	± 7	17.8	0.5	18	59	23
LS	14.5 ± 0.9	± 6	1.1	0.5; 1.0	8	89	4
EUV	16.9 ± 0.6	± 4	3.0	0.9; 18.6	0	67	33
MI	25.9 ± 1.0	± 4	0.9	0.8	6	92	2
MX	27.6 ± 1.3	± 5	1.5	22.4	8	50	43
SA	28.9 ± 0.9	± 3	9.4	0.3; 12.7	17	69	14

The MA stone has a heterogeneous pore network, showing the highest C_D of the investigated stone types (17.8%); the majority of pores (59%) are capillary (r_2). LS shows a bimodal distribution with two families of capillary pores very close to each other, centred on 0.5 and 1.0 μm diameter; the 89% of all the pores are capillary. The EUV stone shows a bimodal distribution, with widely spaced peaks at 0.9 and 18.6 μm, which is mirrored by the pore distribution between r_2 (67%) and r_3 (33%). The unimodal distribution of MI stone is homogeneous (with the only $C_D < 1$ of the investigated series) and centred on $d_{peak} = 0.8$ μm; the capillary pores are almost the entirety (92%) of the MI pore network. The MX stone has a unimodal distribution as well, but centred on a very large d_{peak} (22.4 μm) and much more scattered than MI, featuring the lowest percentage (50%) of capillary pores. Finally, the pore distribution of the SA stone is very scattered ($C_D = 9,4$), with widely spaced peaks at 0.3 and 12.7 μm; the pore families are mainly capillary (69%), but the r_1 and r_3 categories are also present.

Figure 4 compares, individually for each stone, the pore access radius distribution of specimens altered by heating–cooling cycles at 400 and 600 °C to that of unheated stone. Severe thermal stresses through heating–cooling cycles can lead to changes in pore size that differ very much from one limestone to another; there is no generalizable trend of evolution.

The MI stone retains its unimodal pore size distribution at the post-cooling state, with a slight shift of the peak towards larger radii, corresponding to a modest increase in N_T porosity (see Fig. 3).

MA (unimodal and very hererogeneous pore distribution) and LS (bimodal with peaks close to each other) undergo a similar modification of their pore networks, i.e. the creation of new families of pores of larger radius. This phenomenon can be explained by the coalescence of microcracks, caused by thermal expansion, which exerts mechanical stresses greater than the stone can withstand. This modification of the pore morphology is accompanied by an increase in porosity, the more pronounced as the temperature is higher. Thus, the MA stone sees its peak value shifted to 2.43 μm. The same holds for LS stone, whose second peak is shifted from 0.48 μm to 1.22 μm. For SA stone, only the first peak (0.12 μm) is slightly shifted to 0.22 μm.

Finally, EUV and MX show the greatest total porosity gains at 600 °C, however their behaviour is in contrast to the other stones (whose porosities shift towards larger radii after heat treatment). Initially, the EUV stone shows a perfectly balanced bimodal distribution centred in 0.48 μm and 11.53 μm. As for MX, it has a large peak at 11.21 μm, but its high porosity is also widely represented in the range 0.1–10 μm. Within these two stones, new and large families of pores with smaller radii appear. In this sense, part of the porosity of EUV is now located in a pore size range (0.03–0.20 μm) that is absent at the original state; moreover, after exposures to 400 °C and 600 °C a large proportion of porosity is associated to pore sizes larger than 10 μm. For MX, the characteristic radius of its main peak decreases from 11.21 μm to 4.31 μm at 400 °C, and to 3.86 at 600 °C. In addition, there is a localized increase in porosity in the 0.1–1 μm range, which is even greater at higher temperatures.

3.4 SEM observations

The qualitative observations made on thermally altered samples, after exposure to a 600 °C heating–

Fig. 4 Comparison of pore size distribution from MIP, at initial state (20 °C) and after heating–cooling cycles (400 °C and 600 °C)
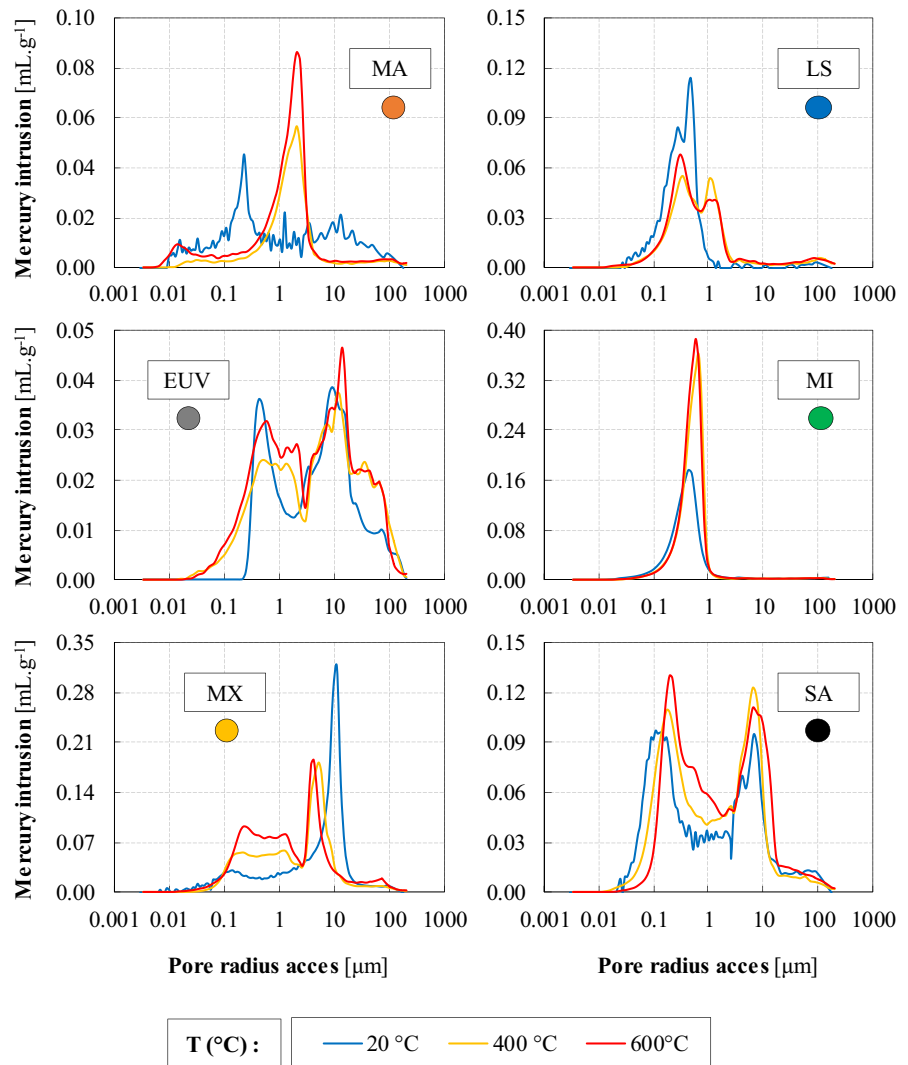
cooling cycle, are compared with those made on untreated stone fragments (Fig. 5).

In the MA limestone at the initial state (Fig. 5a), dense zones are contrasted with more granular zones where pores covering a wide interval (0.1–10 µm) can be identified. These elements corroborate the mercury porosimetry spectra (Sect. 3.3). This is related to the variedness of this stone, which is composed of oolites, peloids and bioclasts, within a matrix classified as mostly microsparite (Table 1). The cracks that can be distinguished on thermally altered stone are located in the matrix and are intergranular.

The comparison of the microstructure of LS limestone before and after alteration (Fig. 5b) reveals intergranular microcracks in the sparitic matrix,

bypassing the peloids. A large and important decohesion between the peloids and the matrix is visible, leading to the detachment and disappearance of these elements. In addition, a new family of pores, around a few µm radii, seems to appear between the interface of the micritic and sparitic matrix. This hypothesis is verified by mercury porosimetry spectra (Sect. 3.3).

The bimodal pore size distribution of EUV limestone, highlighted by the mercury porosimetry analyses (Fig. 4) seems to be related on the one hand to fine and intragranular porosity, and on the other hand to intergranular porosity between sparite crystals, associated with a range of larger pore sizes. The damage caused by the 600 °C heating–cooling cycle on the EUV stone seems to lead to strong cracking
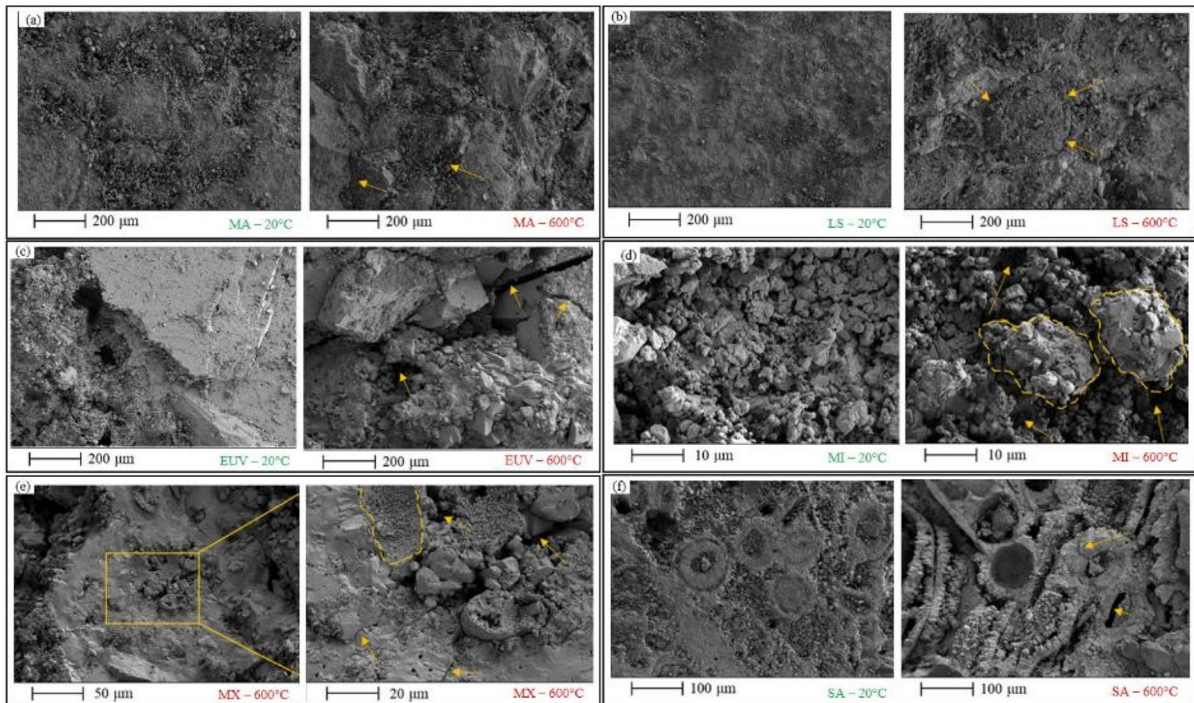
Fig. 5 SEM observations at initial state (20 °C) and after a 600 °C heating–cooling cycle (MX only after 600 °C at different magnification factors)

(intergranular, intragranular and transgranular) of the bioclasts widely present in this material (Fig. 5c). The calcite crystals associated with the sparite matrix also show some decohesion leading to a much lower compactness.

The SEM observations of MI limestone (Fig. 5d) reveal very little alteration caused by the heating–cooling cycle at 600 °C. Only a few intragranular cracks affecting sparite crystals are noticeable. Exposure to heating at 600 °C seems to have a relatively moderate influence on this limestone, which does not show any significant modification of its porous network (Sect. 3.3). This may explain the relatively high level of residual strength of this stone as a function of temperature (Table 7 Appendix).

In MX stone, pores of peak diameter ~ 20 µm, characteristic of an intergranular porosity, are visible in the SEM images at the initial state. The peak diameter for the altered stone tends to decrease, according to the mercury porosimetry spectra; this is observed in the SEM images, where the pores appear relatively smaller (~ 10 µm). Intragranular cracks

are observed on the figured elements of the thermally treated stone (Fig. 5e). In addition, the appearance of new families of fine pores (0.1–1.0 µm) in stones exposed to the heating–cooling cycle, identified in Sect. 3.3, can be observed close to the clusters of micrite and microsparite (peloids).

Thermal damage to the microstructure of SA results in strong alteration, both of the oolites and of the binding phase consisting of sparite and microsparite. The nuclei show traces of significant alteration, or even their total disappearance. The cortex of the oolites is also strongly damaged, where intragranular cracks are observed (Fig. 5f). Large intergranular cracks affecting the microsparite cement are observed as well as possible pore coalescence, which may explain the increase in total porosity ($\sim 4\%$ at 600 °C) determined in Sect. 3.2. Large drusic calcite crystals are also observed but show no evidence of cracking. The relatively high proportion of porosity associated with fine pores (0.1–1 µm) seems to be located in the internal fibrous part of the cortex of the oolites.
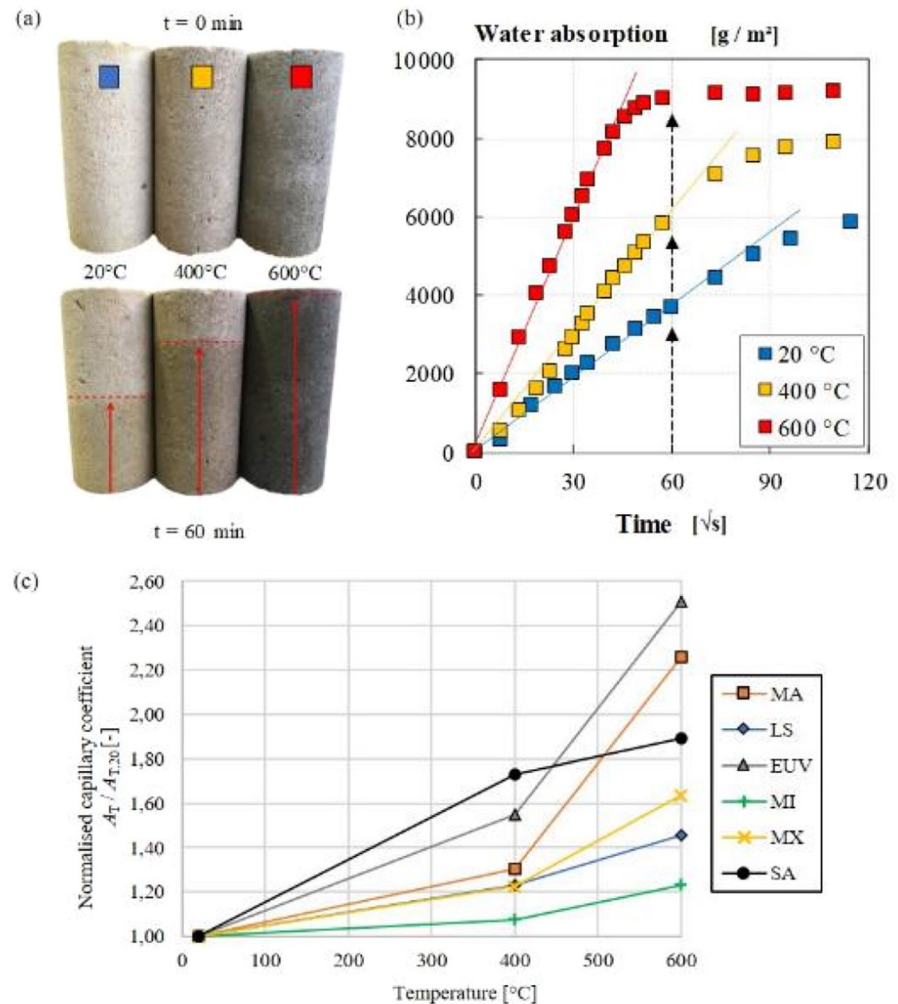
3.5 Capillarity coefficient

Figure 6a–c illustrate the consequences of exposure at 400 and 600 °C on the capillary water absorption capacity of the same limestone.

The EUV limestone, having been subjected to a heating–cooling cycle at 600 °C, absorbs 50% more water (per unit area) than at the original state (Fig. 6a). The absorption kinetics are visibly accelerated by the thermal damage, i.e. after 600 °C 1 h is required to reach a stabilization level, instead of the 4 h for the unaltered stone (Fig. 6b). The decision to carry out this test only on samples exposed to the thermal cycles of 400 and 600 °C is based on the fact that the change in A can be compared to the variations in the porous network, determined experimentally by mercury porosimetry (Sect. 3.3). A similar finding for all the stones studied can be established: exposure to heating–cooling cycles leads to an increase in the capillary absorption coefficient (Fig. 6c).

MI, which has so far shown the best mechanical stability with respect to high temperatures, shows the least relative evolution; the capillary absorption coefficient A, which is very high at the original state (224 g/[m$^2\sqrt{\text{s}}$]), increases to a value of 275 g/[m$^2\sqrt{\text{s}}$] after the 600 °C plateau. MX limestone, which shows an original value close to that of MI (209 g/[m$^2\sqrt{\text{s}}$]), shows a much more pronounced increase at 600 °C, reaching the highest value among all the stones in the study (342 g/[m$^2\sqrt{\text{s}}$]). For the most porous stone, SA (see Table 1), A almost doubles between the original state and after 600 °C, rising from 73 to 138 g/

Fig. 6 Effect of heating–cooling cycles (400 °C and 600 °C) on the water absorption capacity for EUV limestone: **a** visual aspect of water uptake during the test, **b** curves of water absorption versus time for intact (20 °C) and heated specimens (400 °C and 600 °C) and **c** Normalised water absorption coefficient as a function of temperature

$[m^2\sqrt{}/s]$. EUV limestone—whose mechanical strength is highly sensitive to severe thermal exposure (Table 7 in the Appendix)—shows an absolute increase in the capillary absorption coefficient (+ 111 g/[m²√/s]) at 600 °C, an almost triple value than at 20 °C. Finally, MA and LS, which have the lowest total porosity (Table 1), and a relatively low coefficient of capillarity at the original state (22 and 48 g/[m²√/s]), undergo the smallest absolute increase: + 30 g/[m²√/s] for MA, and + 22 g/[m²√/s] for LS. However, this absolute variation corresponds to a significant relative increase (+ 140%) for MA stone at 600 °C, indicating a definite influence of this target temperature. On the contrary, the small relative increase of LS (+ 40%) positions it with MI as the least affected stones.

Different physical and mechanical parameters affect the durability of a material. A high porosity A high porosity—if joined to an increase in capillary pores—facilitates the proneness to weathering-related forms of decay, namely the damage due to freeze–thaw processes in presence of free water inside the pores, and the crystallisation stresses of salts possibly migrating with water [42]. The capillary absorption coefficient plays an important role in the frost sensitivity of stones [43]. Such decay affects the mechanical strength of the material, which must be assessed at the post-fire state in view of the possible loading changes during and after restoration.

All the investigated limestones have shown an increase in porosity after exposure to high temperatures, even after 400 to 600 °C. The relationship of this increase to a potential increase in water absorption capacity is mediated by the modifications in the pore size distribution, enlightened by the MIP pore spectra (Fig. 4). According to some authors, the capillary absorption of water involves only the pores with radius of 0.1 to 10 μm [23], but others propose a larger interval, i.e. 0.1 to 100 μm [44, 45]. The correlation between the MIP porosity (N_{Hg}) and the capillary water absorption coefficient (A) at the initial state for all the six limestones was found statistically significative only in the 0.1–100 μm pore radius interval, with a P-value equal to 0.024 (Table 4).

The graph in Fig. 7 shows the N_{Hg}–A experimental values based on the N_{Hg} porosity in the 0.1 to 100 μm interval of pore radius, at the initial state and after cycles at 400 and 600 °C. For each of the six stones, linear trends $A(N_{Hg}) = mN_{Hg} + q$ are plotted (dotted lines), whose coefficients are listed in Table 5. The

relationships appear reliable for all the stone types except MA.

As well, a power law fit for all the 18 couples of values for all the limestones is plotted (Eq. 7, Fig. 7). It fits well the N_{Hg}–A experimental data for the cases of lowest porosity ($N_{Hg} < 20\%$), meaning MA, LS and, up to 400 °C, EUV; the data are scattered in the range $20\% < N_{Hg} < 35\%$.

$$A(N_{Hg}) = 0.4161 N_{Hg}^{1.8423} \tag{7}$$

3.6 Ultrasonic wave velocity

The normalised compressive strength and P-wave velocity as functions of temperature for the different limestones are shown in Fig. 8a, b.

The EUV limestone, which emerges as the most sensitive stone to high temperatures, as far as the mechanical strength is concerned (Fig. 6a), also shows the greatest loss of P-wave velocity. The 200 °C heating–cooling cycle marks a drop of − 30% in P-wave velocity, while the other stones show no more than − 10%. EUV is also the only stone whose evolution has two distinct phases, i.e. a sharp drop (-60%) before 400 °C and a second phase where the decrease is much softer. For the other types, P-wave velocity changes almost linearly with temperature, with losses between − 40% and − 70% at 800 °C.

In post-fire surveys of stonework buildings, P-wave velocity tests can be very useful in evaluating the residual porosity and strength. After calibration onto N_T or N_{Hg} results, such non-destructive diagnostic procedure would allow extending the experimental information coming from laboratory tests. For the investigated limestones, V_P–N_T relationships are shown in Fig. 9a (dotted lines). The trends of P-wave velocity are clearly descending with increasing total porosity; reliable linear formulations $N_T(V_P) = mV_P + q$ are proposed in Table 6.

Finally, the couples of V_P–R_C experimental values are plotted in the graph of Fig. 9b. $R_C(V_p)$ is a nonlinear function that can be expressed through second order polynomials (Table 6, dotted lines in Fig. 9b). However, as it comes to the samples heated up to 800 °C, the inhomogeneous consistency of the sample—external layer of portlandite—must not be neglected (Fig. 1).

Table 4 Statistical analysis of $N_{Hg}-A$ relation at the unheated state

ID	NHg [%] in the pore radius interval					A [g/(m$^2\sqrt{}$s)]
	0.1–100 μm	0.1–10 μm	0.1–1 μm	1–100 μm	1–10 μm	
MA	8.9	6.6	3.9	5.0	2.7	23
LS	14.1	13.7	13.3	0.8	0.4	48
EUV	16.9	11.5	4.8	12.0	6.7	73
MI	25.0	24.7	23.6	1.4	1.1	224
MX	25.8	14.7	4.3	22.5	10.4	209
SA	24.9	21.2	11.1	13.8	10.1	105
P value of $N_{Hg}-A$ linear regression	0.024	0.111	0.355	0.518	0.624	

Fig. 7 Capillary absorption coefficient A versus porosity N_{Hg} in the pore radius interval 0.1–100 μm
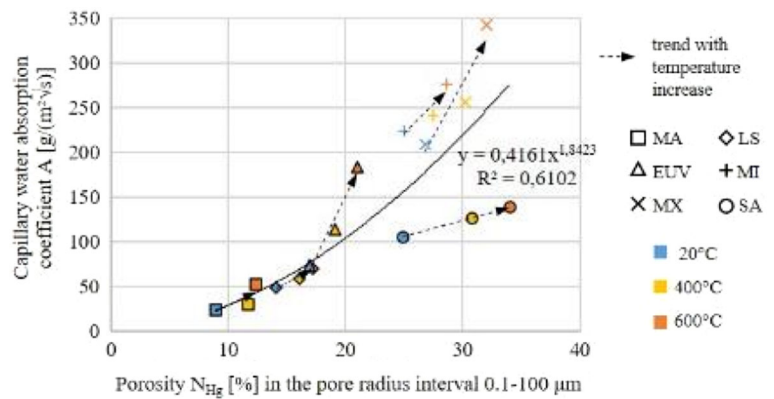
Table 5 Coefficients of the parameter trends for the $A-N_{Hg}$ relationships (Fig. 7)

ID	$A(N_{Hg}) = mN_{Hg} + q$		
	m	q	R^2
MA	6.633	− 37.959	0.659
LS	6.903	− 50.065	0.973
EUV	26.603	− 382.460	0.961
MI	13.134	− 108.060	0.835
MX	24.049	-444.450	0.887
SA	3.618	+ 14.021	0.999

3.7 Colour changes

Figure 10a–c show the images of visual aspect and colour of all the investigated types of stone after the heating–cooling cycles at 200, 400, 600 and 800 °C.

Generally, the 200 °C heating–cooling cycle has not induced any change of colour or visible cracks (Fig. 10a). The 400 °C heating–cooling cycle results in the appearance of a reddish/brown tinge on MA,

EUV, MI and MX limestones, i.e. the phenomenon of rubefaction. After heating up to 600 °C, all the stone types darken, and the brown tint is visible in the background. The MX stone shows the strongest darkening (i.e. lowest $L*$) at 600 °C; the decrease in $L*$ is usually linked to the start of calcite decarbonation, but attains different values even among the limestones of 100% calcite (LS, EUV, MI and SA). The presence of quartz in MX (about the 14%) and possibly that of organic traces (fossil shells) may have had a role. Finally, on all stones heated to 800 °C, large networks of cracks are present; a whitish color appears on the surface of the specimens, corresponding to a thin layer of a few millimeters laterally enveloping the specimen. Nevertheless, the core of the specimen retains the dark color that appears when exposed to 600 °C.

The analysis of the colour changes of the stones due to exposure to high temperatures has highlighted several features with regard to the evolution of colorimetric parameters (Fig. 11a, b).
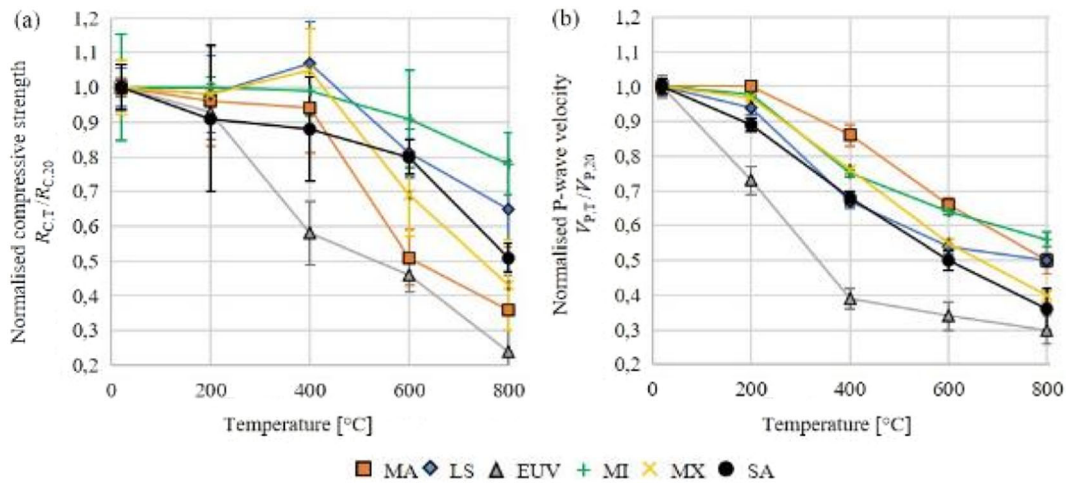
Fig. 8 Relative evolution of **a** compressive strength and **b** P-wave velocity as a function of temperature up to 800 °C
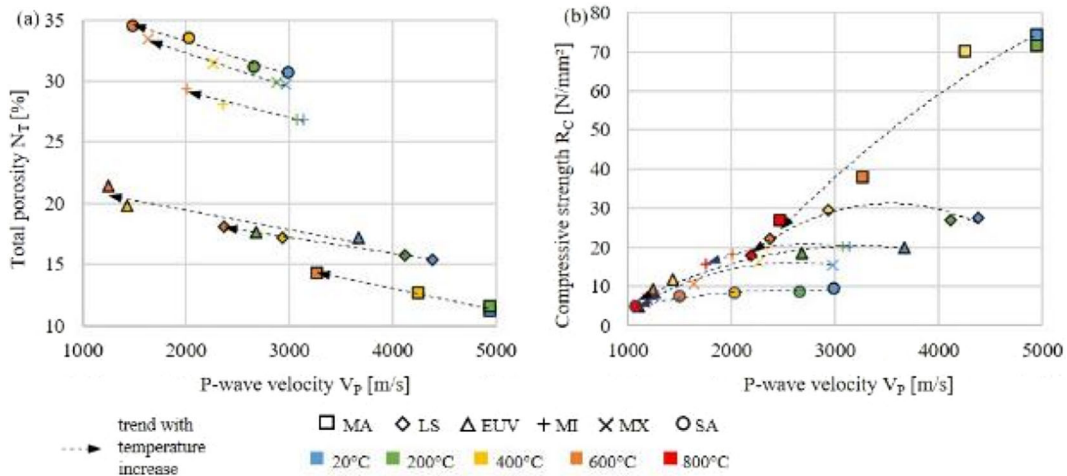

Fig. 9 **a** P-wave velocity versus porosity as a function of temperature, and **b** P-wave velocity versus compressive strength as a function of temperature

Table 6 Coefficients of the parameter trends for the N_T—V_P and R_C—V_P relationships (Fig. 9a-b)

ID	$N_T(V_P) = mV_P + q$			$R_C(V_P) = aV_P^2 + bV_P + c$			
	m	q	R^2	a	b	c	R^2
MA	-1.7×10^{-3}	20.006	0.989	-3×10^{-6}	3.93×10^{-2}	-56.801	0.954
LS	-1.3×10^{-3}	21.095	0.995	-7×10^{-6}	4.96×10^{-2}	-56.231	0.925
EUV	-1.6×10^{-3}	22.670	0.861	-3×10^{-6}	1.98×10^{-2}	-11.640	0.966
MI	-2.1×10^{-3}	33.349	0.966	-5×10^{-6}	2.84×10^{-2}	-18.111	0.991
MX	-2.7×10^{-3}	37.790	0.996	-5×10^{-6}	2.58×10^{-2}	-17.350	0.976
SA	-2.7×10^{-3}	38.717	0.979	-1×10^{-6}	0.79×10^{-2}	-1.673	0.921

Fig. 10 Visual aspect and color change of all limestone specimens (**a**) after the different heating–cooling cycles; details of rubefaction in EUV (**b**) and darkening in MX (**c**)
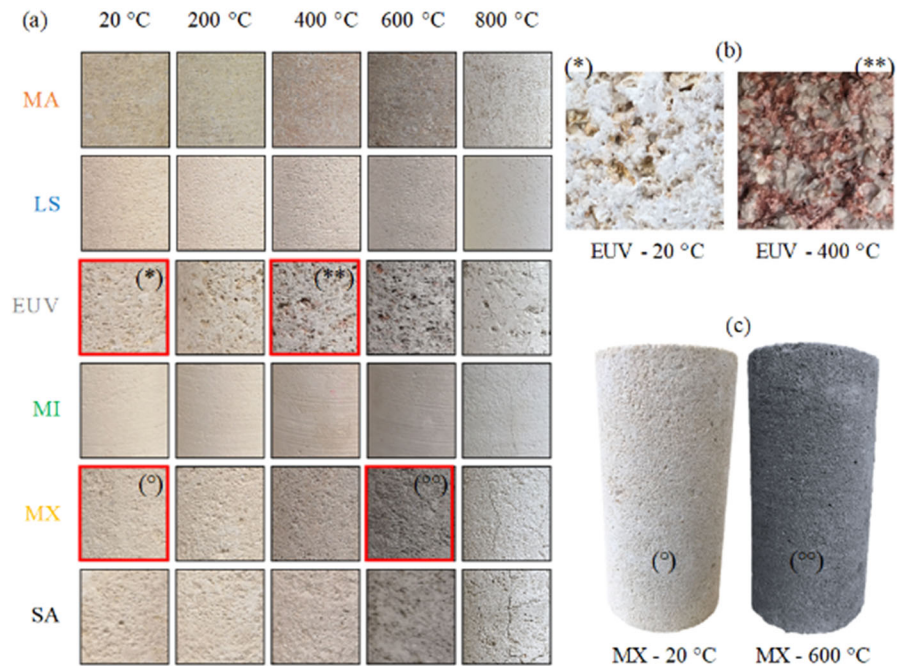
The following facts are common to all the limestones tested.

- A rise in temperature leads to a global joint decrease in the values of the parameters a^* and b^*.
- The appearance of a reddening (rubefaction phenomenon) of the stone as early as 250 °C, due to the dehydration of goethite (iron hydroxyde), corresponds to an increase in the parameter a^*, equivalent to a positive Δa^* difference (Fig. 11a). Nevertheless, its visual perception at 400 °C gradually fades and is no longer clearly identifiable at 600 °C.
- The darkening of the stone, i.e. a progressive decrease of the parameter L^* is accompanied by a disappearance of colour tints (decrease of a^* and b^*) until the beginning of the calcite decarbonation.
- The formation of lime, through the decomposition of calcite, leads to a whitening of the stone (dramatic increase in L^*). Furthermore, it is interesting to note that all the limestones, regardless of their original colour, show a lightness value L^* after exposure to 800 °C, which tends to stabilize around 91.26 ± 1.64 (Fig. 11b).

In the perspective of post-fire evaluation of a stonework building, the information from colorimetry provide useful indicators to evaluate the temperature level reached by the stone.

Two out of six types of stones (LS and SA) have shown a decreasing monotonic relationship of Δa^* with temperature (Fig. 9a). For such types, the colorimetric data could be sufficient to define colour-temperature relationships allowing to evaluate the maximum experienced temperature in the range 20–800 °C. However, it must be noted that non negligible colour differences at the original state are possible even within the same stone type, and a full generalisation of these results is not possible. The other four types (MA, EUV, MI, and in a slighter way MX) have shown rubefaction as a consequence of the exposure to 400 °C. The phenomenon is due to the process of dehydroxilation of silicates and clay minerals present at the original state, resulting in the formation of iron oxides. It must be noted that the presence of iron minerals or oxides (see Sect. 3.1 above), at the origin of reddening, had not been detected by the XRD analyses in any of the stones throughout the thermal cycles. Depending on the involved minerals, dehydroxilation can begin at very different temperatures—200 to 500 °C [8]—and develop within different temperature ranges. Throughout this transformation, the changes in a^*, b^* and L^* neither have uniform trends nor direct relationship to
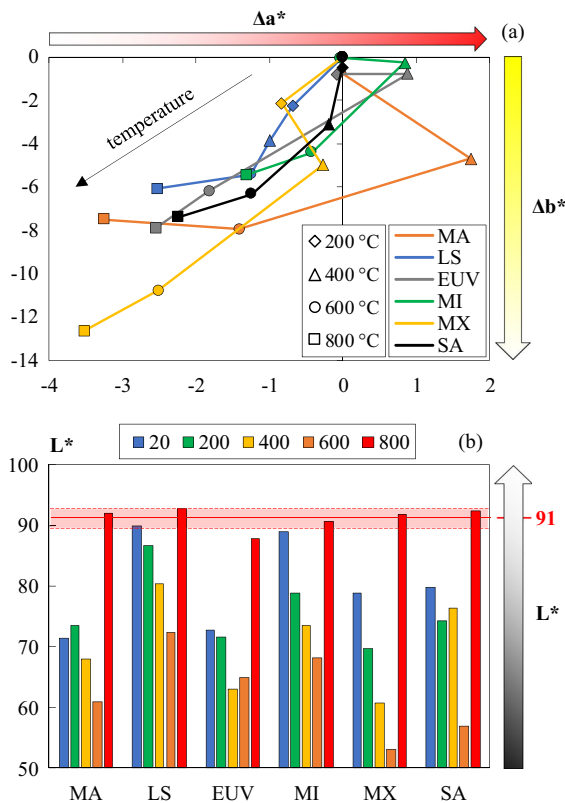
Fig. 11 Evolution of colorimetric parameters as a function of temperature up to 800 °C for limestones: **a** $\Delta a*$ versus $\Delta b*$; **b** $L*$

the temperature [46]. This introduces uncertainties in evaluating the maximum experienced temperature of a fire-exposed element showing rubefaction.

In the four cases observed, the rubefaction measured by colorimetric data appears between 200 and 400 °C and is not visible anymore at 600 °C. Within that temperature range, three of four types (MA, MX and most of all EUV) suffer substantial decrease in mechanical strength (Table 7 in Appendix, Fig. 8a); in real cases, it is thus very important to evaluate the maximum experienced temperature. The plots of Fig. 11a should be refined in the intervals 200–400 °C (EUV) and 400–600 °C (MA and MX), with more tests to define the start and end of rubefaction. As well, other investigation techniques, if viable—e.g. thermogravimetric analysis or infrared spectroscopy [18, 47]—could provide useful and more precise information about the contained minerals undergoing hydroxilation.

3.8 Evolution of the damage state

The evolution of the post-fire state of limestones after cooling, is essential with regard to the safety measures and restoration works to be undertaken. Therefore, a follow-up of the state of damage was carried out on the specimens after exposure to the heating and cooling cycle at 800 °C. The six limestones were examined at their original state, then at 30 min after the end of cooling and finally 24 h later, after preservation at 20 ± 1 °C and 50% RH (Fig. 12). It must be noted that the presented results do not account for any effects of heating rate and initial water content in the samples.

It is worth to remind that 30 min after the end of the heating–cooling cycle at 800 °C, the MA, LS and MI stones show compressive strength higher values than 15 MPa (27, 18 and 16 MPa respectively) while the EUV, MX and SA limestones do not resist higher values than 7 MPa (Table 7 in Appendix).

After 24 h in controlled conditions, all the limestones appear very affected (Fig. 12), from mass loss by superficial crumbling to severe decohesion of the material leading to disintegration.

The preliminary drying of samples and the temperature control allow excluding any effect of humidity or inhomogeneous temperature distribution inside the samples during the heating–cooling cycles. Then, the observed damage, progressing from the surface to the core of the samples, is due to rehydration process, enhanced by the increased capillary porosity and possibly in combination with pre-existing thermally-induced micro-cracks. The decay conditions of all the samples after 24 h were too severe to allow for any measurement of mass uptake, which would have been a descriptor of the entity of rehydration. Additionally, the differences in the decay kinetics are possibly in relationship with the initial mechanical performance and porosity of the stone; MA and LS, which are the two strongest and the least porous types at the original conditions, show the lowest level of belated damage.

4 Conclusions

4.1 Most relevant lessons for practice

After the attack of fire, diagnostic procedures on historic stonework buildings typically include non-destructive tests on site, like P-wave ultrasonic velocity

Fig. 12 Effect of the 800 °C heating–cooling cycle on limestone specimens ($\Phi 4 \times 8$ cm): at initial state (t_0); 30 min after being removed from the furnace ($+ \frac{1}{2}$ h); after 24-h exposure in a monitored room at 50% and 20 °C (24 h). Red lines correspond to macroscopic cracks

measurement and colorimetry. Such procedures are cost-effective and can cover large portions of the damaged building. Indeed, the changes in colour and the decrease in P-wave velocity provide valuable information about the withstood temperatures and the state of damage of stone materials (see Sect. 4.2 below).

However, non-destructive diagnostic techniques have a limited penetration depth, which can be insufficient to obtain a satisfactory level of knowledge in the cases of massive structures. In particular, such techniques are not suitable to detect the water content at the core of structures—which can trigger damage from salts crystallization and freeze–thaw cycles, as it was noticed in a recent paper about the issues of post-fire restoration on Notre Dame de Paris [11]. For this reason, laboratory tests are often essential in providing quantitative information. The residual porosity, pore size distribution and capillary water absorption coefficient—as well as the main mechanical parameters—can only be assessed by sacrificing small material samples and are essential as a basis for judgement on the durability of stonework affected by fire damage.

The effectiveness of diagnostics would be maximised if correlations can be established between parameters from destructive and non-destructive tests. The qualitative information typically provided by detected colour and P-wave velocity, if robustly linked to quantitative information—e.g. related values of withstood temperature, residual porosity and strength—can extend the validity of the latter within the investigated structure; in this way, it is possible to obtain a quantitative picture of damage with limited micro-destructive sampling.

The presented research demonstrates that it is difficult to find general trends of temperature-

dependent properties for limestones, while the results show clear trends for the single types. This is particularly important in the field of post-fire restoration. In fact, the technique of stone replacement is more likely to be accepted than application of other materials (e.g. ethyl silicate) to restore the strength of stonework, since it allows for a better approach to the need for authenticity [11]. Thus, the presented results enlighten crucial properties for the choice of the best stone types for replacement. Aside from the mechanical properties (in particular the stiffness) and thermal expansion, the water absorptivity is essential in ensuring compatibility between the original and new materials.

Finally, integrated (on site + in lab testing) strategies would also be useful in pursuing a sustainable management of cultural heritage assets. The adoption of plans of periodic investigations is advisable after restorations [11].

4.2 Concluding remarks

Construction limestones feature a great variety of properties; this study has taken into consideration six French limestones of different density, porosity, absorptivity and strength, whose characterisation has been performed through the 200–800 °C range.

The features of temperature-induced damage (immediately after cooling) are also very variable across the investigated species. After exposure to 800 °C, the least heat-sensitive stone (Migné, MI) has shown a − 22% of original strength, negligible changes in the pore size distribution and the lowest increases in total porosity (+ 2.5%) and capillarity coefficient (+ 20%); the SEM observation have enlightened a limited intergranular cracking. Vice versa, the most heat-sensitive stone (Euville, EUV) has undergone − 76% of original strength, the appearance of new capillary pores, the highest increases in total porosity (+ 4%) and capillarity coefficient (+ 150% of the original value); the SEM observation have enlightened intergranular, intragranular and transgranular cracking. The changes in the other stones lie between these two behaviours.

The colorimetric analyses allowed establishing specific characteristics of the temperature-dependent colour change in the investigated limestones. On the other hand, it would be opportune to define more precisely the temperature interval of the rubefaction phenomenon.

For each of the investigated stones, the total porosity N_T showed reliable linear correlations with the temperatures of the heating–cooling cycles (20–800 °C). These relations could be useful in associating specific residual porosity values to the temperatures that could be detected by colorimetry.

Between the experimental values of porosity N_{Hg} measured by means of MIP in the pore radius interval 0.1–100 μm (corresponding to capillary pores) and the capillary water absorption coefficient A, a significant correlation (P value < 0.05) was ascertained. As well, a nonlinear general relation (based on all the data of all the stone species) was searched and proven valid only in the low range of density. Linear N_{Hg}–A relationships for the single species are all significant except for the Massangis (MA) stone.

As well, nonlinear relationships for each type of stone—in the investigated temperature field—were demonstrated between the P-wave velocity V_P and the compressive strength R_C; as well, linear relationships hold between the P-wave velocity V_P and total porosity N_T. These equations could enhance the usefulness of non-destructive testing (ultrasonic tests on site) in cases featuring the investigated stones.

Finally, attention was paid to the visible evolution of decay of the limestone species after a thermal cycle at 800 °C and subsequent cooling. After 24 h in controlled conditions of 20 °C and 50% RH, all the limestone samples—even the types with highest residual strength immediately after cooling—showed a very clear progress in decay. This is indeed due to the enhanced proneness to weathering and reduced mechanical effectiveness as direct consequences of the modification of the materials' porous network. The mass loss must thus be considered for stonework structural parts experiencing temperatures > 700 °C and exposed to environmental actions.

Declarations

Conflict of interest The authors declare that they have no conflict of interest.

Appendix

See Table 7.

Table 7 Uniaxial compressive strength after high temperature exposure

Mean uniaxial compressive strength [N/mm^2]

ID	20 °C	200 °C	400 °C	600 °C	800 °C
MA	74.5 ± 1.5	71.5 ± 9.3 (− 4%)	70.0 ± 9.1 (−− %)	38.0 ± 3.0 (− 49%)	27.1 ± 4.9 (− 64%)
LS	27.5 ± 1.5	27.0 ± 3.0 (− 2%)	29.4 ± 3.5 (+ 7%)	22.3 ± 1.6 (− 19%)	17.9 ± 2.6 (− 35%)
EUV	20.0 ± 0.5	18.6 ± 1.5 (− 7%)	11.6 ± 1.0 (− 42%)	9.2 ± 0.5 (-54%)	4.8 ± 1.1 (− 76%)
MI	20.1 ± 3.1	20.1 ± 0.6 (0%)	19.9 ± 1.4 (− 1%)	18.3 ± 2.6 (− 9%)	15.7 ± 1.4 (− 22%)
MX	15.5 ± 1.2	15.2 ± 0.3 (− 2%)	16.3 ± 2.0 (+ 5%)	10.7 ± 1.3 (− 31%)	6.7 ± 0.9 (− 57%)
SA	9.4 ± 0.6	8.6 ± 1.8 (− 9%)	8.3 ± 1.2 (− 12%)	7.5 ± 0.4 (− 20%)	4.8 ± 0.2 (− 49%)

References

1. Tandon A (ed) (2018) First Aid to cultural heritage in times of crisis—1. ICCROM, Rome
2. Pereira D (2019) Natural stone and World Heritage: Salamanca. CRC Press/Balkema, Leiden
3. Kaur G, Singh SN, Ahuja A, Singh ND (2020) Natural stone and World Heritage: Delhi-Agra (India). CRC Press/Balkema, Leiden
4. Davis M (2021) Fire-ravaged Royal Clarence Hotel site derelict five years on. https://www.bbc.com/news/uk-england-devon-59062937. Accessed 23 Feb 2022
5. Kincaid S (2020) After the fire: reconstruction following destructive fires in historic buildings. Hist Environ Policy Pract 11(1):21–39
6. Smith J, Gomez-Heras M, Viles HA, Cassar J (2010) Limestone in the built environment: present-day challenges for the preservation of the past. Geol Soc Spec Publ 331:1
7. Cassar J, Winter MG, Marker BR et al (2014) Introduction to stone in historic buildings: characterization and performance. Geol Soc Spec Publ 391:1–5
8. Sippel J, Siegesmund S, Weiss T et al (2007) Decay of natural stones caused by fire damage. Geol Soc Spec Publ 271:139–151
9. Robert F, Colina H (2008) The influence of aggregates on the mechanical characteristics of concrete exposed to fire. Mag Concr Res 61:311–321
10. Sciarretta F, Eslami J, Beaucour AL, Noumowé A (2021) State-of-the-art of construction stones for masonry exposed to high temperatures. Constr Build Mater 304:124536
11. Praticò Y, Ochsendorf J, Holzer S, Flatt RJ (2020) Post-fire restoration of historic buildings and implications for Notre-Dame de Paris. Nat Mater 19:817–820
12. Concu G, De Nicolo B, Valdes M (2014) Prediction of building limestone physical and mechanical properties by means of ultrasonic P-Wave velocity. Sci World J 2014:508073
13. Ince I, Bozdağ A, Tosunlar MB et al (2018) Determination of deterioration of the main facade of the Ferit Paşa cistern by non-destructive techniques (Konya, Turkey). Environ Earth Sci 77:420
14. Beck K, Janvier-Badosa S, Brunetaud X et al (2016) Non-destructive diagnosis by colorimetry of building stone subjected to high temperatures. Eur J Environ Civ Eng 20(6):643–655
15. EN (2013) Natural stone test methods. Determination of resistance to ageing by thermal shock, EN 14066:2013
16. Franzoni E, Sassoni E, Scherer GW, Naidu S (2013) Artificial weathering of stone by heating. J Cult Herit 14S:e85–e93
17. RILEM TC 129-MHT (1995) Test methods for mechanical properties of concrete at high temperatures—compressive strength for service and accident conditions. Mater Struct 28:410–414
18. Vigroux M, Eslami J, Beaucour AL et al (2021) High temperature behaviour of various natural building stones. Constr Build Mater 272:121629
19. Luque A, Ruiz-Agudo E, Cultrone G et al (2011) Direct observation of microcrack development in marble caused by thermal weathering. Environ Earth Sci 62:1375–1386
20. Koca MY, Ozden G, Yavuz AB et al (2006) Changes in the engineering properties of marble in fire-exposed columns. Int J Rock Mech Min Sci 43:520–530
21. Pires V, Rosa LG, Dionisio A (2014) Implications of exposure to high temperatures for stone cladding requirements of three Portuguese granites regarding the use of dowel–hole anchoring systems. Constr Build Mater 64:440–450
22. NF EN 1936 (2007) Méthodes d'essai des pierres naturelles—Détermination des masses volumiques réelle et apparente et des porosités ouvertes et totale
23. Çelik MY, Kaçmaz AU (2016) The investigation of static and dynamic capillary by water absorption in porous building stones under normal and salty water conditions. Environ Earth Sci 75:307
24. Tomašić I, Lukić D, Peček N, Kršinić A (2011) Dynamics of capillary water absorption in natural stone. Bull Eng Geol Environ 70:673–680
25. Benavente S, Such-Basañez I, Fernandez-Cortes A et al (2021) Comparative analysis of water condensate porosity using mercury intrusion porosimetry and nitrogen and water adsorption techniques in porous building stones. Constr Build Mater 288:123131
26. Cnudde V, Cwirzen A, Masschaele B, Jacobs PJS (2009) Porosity and microstructure characterization of building stones and concretes. Eng Geol 103:76–83
27. Alessandri C, Mallardo V (2012) Structural assessments of the Church of the Nativity in Bethlehem. J Cult Herit 13:e61–e69

28. Bosiljkov V, Uranjek M, Žarnić R, Bokan-Bosiljkov V (2010) An integrated diagnostic approach for the assessment of historic masonry structures. J Cult Herit 11:239–249

29. Carpinteri A, Lacidogna G, Invernizzi S et al (2009) Stability of the vertical bearing structures of the Syracuse cathedral: experimental and numerical evaluation. Mater Struct 42:877–888

30. De Kock T, Dewanckele J, Boone M et al (2014) Replacement stones for Lede stone in Belgian historical monuments. Geol Soc Spec Publ 391:31–46

31. Lopez-Arce P, Tagnit-Hammou M, Menendez B et al (2016) Physico-chemical stone-mortar compatibility of commercial stone-repair mortars of historic buildings from Paris. Constr Build Mater 124:424–441

32. Dunham RJ (1962) Classification of carbonate rocks according to depositional texture. In: Ham WE (ed) Classification of carbonate rocks: a symposium. American Association of Petroleum Geologists Memoir, pp 108–121

33. Beck K (2006) Etude des propriétés hydriques et des mécanismes d'altération des pierres calcaires à forte porosité. PhD Dissertation, Université d'Orléans [in French]

34. Sciarretta F, Fava S, Francini M et al (2021) Ultra-high performance concrete (UHPC) with polypropylene (Pp) and steel Fibres: investigation on the high temperature behaviour. Constr Build Mater 304:124608

35. Rietveld HM (1969) A profile refinement method for nuclear and magnetic structures. J Appl Crystallogr 2:65–71

36. Darley JJ, Lott JNA (1973) Low temperature freeze-drying for the scanning electron microscope using liquid nitrogen at low vacuum. Micron 4:178–182

37. Di Remigio G, Rocchi I, Zania V (2021) Scanning Electron Microscopy and clay geomaterials: from sample preparation to fabric orientation quantification. Appl Clay Sci 214:106249

38. Rahmouni A, Rhaffari YEL, Boulanouar A et al (2017) Effect of porosity and water saturation on the mechanical properties and P-wave velocity of calcarenite rocks used in the construction of historical monuments in Rabat, Morocco. In: Proceedings of 13ème Congrès de Mécanique, Meknès, Morocco

39. Razafinjato RN, Beaucour AL, Hébert R et al (2013) Thermal stability of different siliceous and calcareous aggregates subjected to high temperature. In: MATEC web of conferences, vol 6, pp 1–9

40. Walbert C, Eslami J, Beaucour AL et al (2015) Evolution of the mechanical behaviour of limestone subjected to freeze-thaw cycles. Environ Earth Sci 74:6339–6351

41. Remy JM (1993) Influence de la structure du milieu poreux carbonaté sur les transferts d'eau et les changements de phase eau-glace: application à la durabilité au gel de roches calcaires de Lorraine. PhD Thesis, Institut National Polytechnique de Lorraine (French)

42. McCabe S, Smith BJ, Warke PA (2010) Exploitation of inherited weakness in fire-damaged building sandstone: the 'fatiguing' of 'shocked' stone. Eng Geol 115:217–225

43. Eslami J, Walbert C, Beaucour AL et al (2018) Influence of physical and mechanical properties on the durability of limestone subjected to freeze-thaw cycles. Constr Build Mater 162:420–429

44. Benavente D (2011) Why pore size is important in the deterioration of porous stones used in the built heritage. Rev Soc Esp Miner 15:41–42

45. Siegesmund S, Snethlage R (eds) (2011) Stone in architecture. Springer, Berlin

46. Hajpál M, Török A (2004) Mineralogical and colour changes of quartz sandstones by heat. Environ Geol 46:311–322

47. Lawrence RMH, Mays TJ, Walker P, D'Ayala D (2006) Determination of carbonation profiles in non-hydraulic lime mortars using thermogravimetric analysis. Thermochim Acta 444:179–189